京都大学
KYOTO UNIVERSITY

KURENAI 紅
Kyoto University Research Information Repository

Contents lists available at ScienceDirect

Journal of Theoretical Biology

journal homepage: www.elsevier.com/locate/yjtbi

ELSEVIER

Check for updates

Cell-center-based model for simulating three-dimensional monolayer tissue deformation

Tomohiro Mimura, Yasuhiro Inoue [*]

Department of Micro Engineering, Graduate School of Engineering, Kyoto University, 615-8540 Kyoto, Japan

ARTICLE INFO

ABSTRACT

The shape of the epithelial monolayer can be depicted as a curved tissue in three-dimensional (3D) space, where individual cells are tightly adhered to one another. The 3D morphogenesis of these tissues is governed by cell dynamics, and a variety of mathematical modeling and simulation studies have been conducted to investigate this process. One promising approach is the cell-center model, which can account for the discreteness of cells. The cell nucleus, which is considered to correspond to the cell center, can be observed experimentally. However, there has been a shortage of cell-center models specifically tailored for simulating 3D monolayer tissue deformation. In this study, we developed a mathematical model based on the cell-center model to simulate 3D monolayer tissue deformation. Our model was confirmed by simulating the in-plane deformation, out-of-plane deformation, and invagination due to apical constriction.

1. Introduction

Cell dynamics mediates the morphogenesis of tissues and organs in living organisms. Cell division and apical constriction actively contribute to morphogenesis. Timing and the anisotropy of cell division can often influence tissue-folding patterns (Adachi et al., 2018). Apical constriction refers to the interactions between actin and myosin accumulated on the apical side of the cell. These interactions exert contractile forces and cause the cell to become wedge shaped (Martin and Goldstein, 2014). Examples of apical constriction-driving organ morphogenesis include gastrulation (Lee and Harland, 2007) and neurulation (Lowery and Sive, 2004).

Various mathematical modeling and simulation studies have been conducted to elucidate the morphogenetic mechanisms based on cellular interactions. Here, we discuss two models that can handle the discreteness of cells. One simulation method that can address the discrete nature of cells is the vertex model, which represents cells as polyhedral in three-dimensional (3D) simulations (Honda et al., 2004; Okuda et al., 2013b) and as polygons in 2D simulations (Fletcher et al., 2014; Alt et al., 2017). Because the vertex models can describe all degrees of freedom involved in morphological changes, they are useful for simulating biological processes at a microscopic scale (Inoue et al., 2016; Inaki et al., 2018). However, modeling individual cells as polyhedral requires many degrees of freedom and substantial computational resources. Moreover, the geometric locations of the polyhedral vertices from the experimental data is extremely difficult to determine. These drawbacks limit suitability of 3D vertex models for predicting or estimating biological parameters involved in specific morphogenetic processes.

The cell-center model (Meineke et al., 2001; Szabó et al., 2006; Pathmanathan et al., 2009; Osborne et al., 2010; Li and Sun, 2014; Lomas, 2014; Soumya et al., 2015; Bi et al., 2016; Barton et al., 2017; Bonilla et al., 2020) is another model that can handle cellular discreteness. This model is suitable for treating phenomena involving cell migration, such as wound healing (Antunes et al., 2013; Brugués et al., 2014) and tumor invasion (Metzcar et al., 2019), in which the cell center continuously changes over time. In this study, we focus on the mechanics of epithelial monolayers. The shape of the epithelial monolayer is represented as a curved tissue in 3D space, where individual cells are tightly adhered to each other. Consequently, the shape of the individual cells affects the morphology of the tissue. Because cell centers alone cannot represent this structure, Delaunay triangulation and Voronoi tessellation are commonly used to establish cell shape. However, these methods require fulfillment of the empty circle property. Therefore, with point set coordination changes, it is necessary to assess whether the constraint condition is met, while maintaining the consistent adjacency relationships of the cells. This is because the circumcenter of an obtuse triangle can be outside of the triangle itself. To avoid this complexity, we adopt the use of the center of mass to represent cell shape, as explained in a later section. Unlike using the circumcenter of a triangle, the center of mass is always inside the triangle.
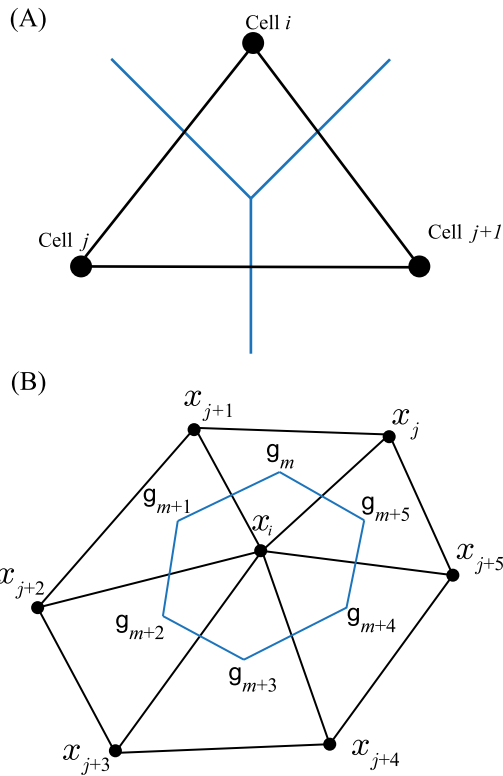
Fig. 1. (A) Definition of a triangular element. Under the condition that three cells are in contact with each other, it is possible to construct a triangular element by connecting neighboring cell centers. The blue lines are cell boundaries and the dots represent cell centers. And the black line connecting their adjacencies makes a triangle. (B) Definition of the shape of cell i. $\boldsymbol{x}_i$ is the position vector of cell i. The cells connected to cell i are denoted j to $j + 5$ counterclockwise. The polygon connecting the centers of mass $\boldsymbol{g}_m$ to $\boldsymbol{g}_{m+5}$ of these triangles is defined as the shape of cell i.

Recent advances in live-cell staining and imaging techniques have enabled real-time observation of cell nuclei in tissue samples. Additionally, researchers have been developing bioprinting (Murphy and Atala, 2014), a technology that builds 3D biological constructs from induced pluripotent stem cells (SCs) (Romanazzo et al., 2019). These technologies can help to elucidate the mechanisms of morphogenesis. The knowledge gained will open the door to tissue engineering applications. For this purpose, we need a 3D mathematical model that assimilates nuclear position data to predict tissue morphogenesis.

The main objective of this study is to create a new 3D mathematical model of tissue morphogenesis, which conceptually differs from the so-called "vertex models", in which cells constituting a tissue sheet are represented by polygons or polyhedral. Our simplified model represents cells as points in 3D space, but does not include terms describing structural changes. This model is an extension of the cell center model to address 3D tissue deformation and is evaluated for its ability to simulate in-plane deformation, out-of-plane deformation, and invagination resulting from apical constriction.

2. Cell-center-based model

In the proposed model, individual cells constituting an epithelial sheet are represented as points in the same manner as in cell-center-based models (Meineke et al., 2001; Szabó et al., 2006; Pathmanathan et al., 2009; Osborne et al., 2010; Li and Sun, 2014; Lomas, 2014; Soumya et al., 2015; Bi et al., 2016; Barton et al., 2017; Bonilla et al., 2020). As defined in Fig. 1(A), under the condition that three cells are in contact with each other, it is possible to construct a triangular element by connecting neighboring cell centers. The epithelial sheet is
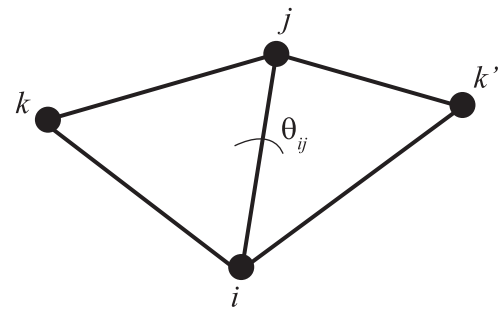

Fig. 2. Angle θ_{ij} around the edge shared by two triangles. i, j, k, and k' indicate cells.

represented as a network of triangular elements formed by connecting adjacent points. Based on this framework, we mathematically express the cell shape, motion, intercalation, division, and apical constriction as described in the following section.

2.1. Cell shape representation

Cell shape is represented by the 2D contour of a cell projected on the neutral plane of the epithelial sheet. To express the shape of cell i, we define a polygon connecting the center of mass $\boldsymbol{g}_m$ of each triangle m that shares cell i (Fig. 1(B)). In this model, cell shape is used for the calculation of cell divisions and rearrangements.

2.2. Equation of the cell motion of each cell

By omitting the inertia term, we can express the equation of motion of cell i as follows:

$$\eta \frac{d \boldsymbol{x}_i}{dt} = -\nabla_{\boldsymbol{x}_i} E \tag{1}$$

where η is the cell point friction coefficient, $\boldsymbol{x}_i$ is the position vector of cell i, and E is the energy function of the system.

The energy function E is the sum of the mechanical energy E_{Mech} of the network of triangular elements and the constraint energy E_{Center} required to satisfy the constraints of cell center:

$$E = E_{\text{Mech}} + E_{\text{Center}} \tag{2}$$

The mechanical energy function E_{Mech} consists of edge length elastic energy E_L, triangular surface elastic energy E_S, dihedral angle elastic energy E_D, apical constriction energy E_{apical}, cell repulsion energy E_{Rep}, and out-of-plane deformation restraint energy E_Z:

$$E_{\text{Mech}} = E_L + E_S + E_D + E_{\text{apical}} + E_{\text{Rep}} + E_Z \tag{3}$$

The edge length energy E_L is the sum of a quadratic energy function that brings the edge length L_{ij} between two adjacent cells i and j close to the equilibrium edge length L_{eq}, using the edge length elastic constant K_L:

$$E_L = \sum_{\langle i,j \rangle} \frac{1}{2} K_L (L_{ij} - L_{\text{eq}})^2 \tag{4}$$

where $\langle i, j \rangle$ below the summation symbol implies all edges connecting two adjacent cells. The triangular area elastic energy E_S is the sum of the quadratic energies that keep the triangle area A_{ijk} formed by cells i, j, and k to the equilibrium triangle area A_{eq}, using the triangular area elastic constant K_S:

$$E_S = \sum_{\langle i,j,k \rangle} \frac{1}{2} K_S (A_{ijk} - A_{\text{eq}})^2 \tag{5}$$

where $\langle i, j, k \rangle$ below the summation symbol indicates all triangles among the three adjacent cells. The dihedral angle elastic energy E_D (a surrogate for bending stiffness) is the sum of the quadratic energies

T. Mimura and Y. Inoue

Journal of Theoretical Biology 571 (2023) 111560

A Self-archived copy in
Kyoto University Research Information Repository
https://repository.kulib.kyoto-u.ac.jp

京都大学
KYOTO UNIVERSITY

京都大学学術情報リポジトリ
KURENAI 紅
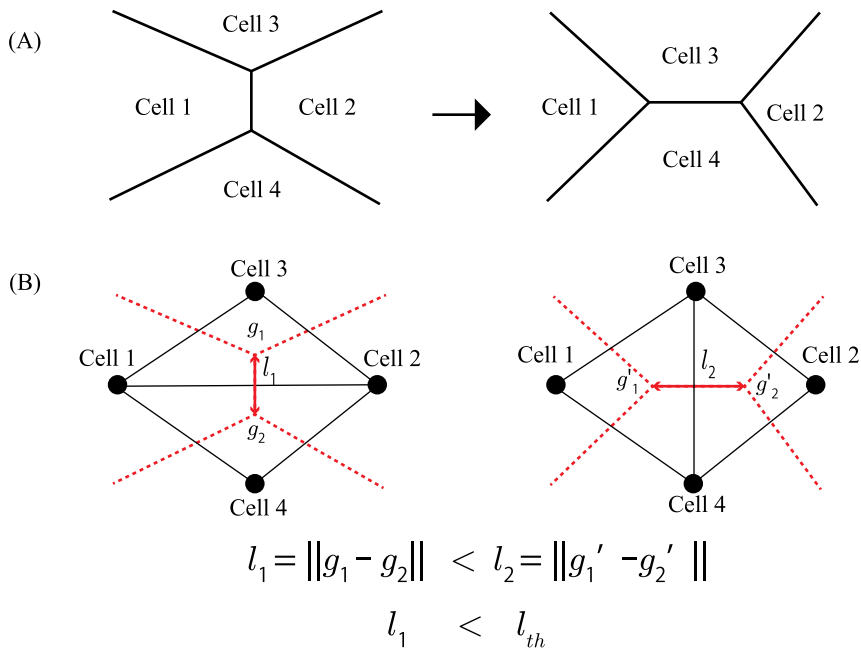Kyoto University Research Information Repository

Fig. 3. (A) Cell intercalation. Cell 3 and cell 4 interrupt cell 1 and cell 2, and the adhesive relationship is updated to cell 3 and cell 4. (B) Representation of flipping. A flip is performed only when the distance between the centers of mass of the two triangles (l_1) is less than the length threshold (l_{th}) and the length before the flip (l_1) is shorter than that after the flip (l_2). l_2 is the expected length assuming a flip has occurred. The position of the cell point does not move with the flip. After the flip, a cool time is set during which the flip does not occur for the duration of τ_{ct}.

that keep the dihedral angle θ_{ij} formed by two triangles sharing the edge between cells i and j (Fig. 2) to the equilibrium dihedral angle θ_{eq}, using the dihedral angle elastic constant K_D:

$$E_D = \sum_{\langle i,j \rangle} \frac{1}{2} K_D (\theta_{ij} - \theta_{eq})^2 \qquad (6)$$

The apical constriction energy E_{apical} brings the adjacent vertex position vectors g_m and $g_{m'}$ of the cell shape closer together when apical constriction occur at the edge $m - m'$. We will explain in detail in 2.5.

$$E_{apical} = \frac{1}{2} K_{apical} \| g_m - g_{m'} \|^2 \qquad (7)$$

where K_{apical} is the apical constriction constant. The cell repulsion energy E_{Rep} is the sum of the energies that keep the distance r_{ij} between cells i and j to cut-off distance r_c when r_{ij} is smaller than r_c.

$$E_{Rep} = \begin{cases} \sum_i \sum_{j<i} \frac{1}{2} K_{Rep} (\frac{r_{ij}}{r_c} - 1)^2 & (r_{ij} < r_c) \\ 0 & (r_{ij} \ge r_c) \end{cases} \qquad (8)$$

where K_{Rep} is the cell repulsion constant. The out-of-plane deformation restraint energy E_Z represents the sum of the energies restricts the z displacement d_{iz} of cell i from its initial position. In this case, it is weighted by the area S_i of cell i and the out-of-plane deformation constraint constant K_Z. S_i is defined as $S_i = \frac{1}{3} \sum_m A_m \cdot n_i$. Here, the normal unit vector n_i at cell i is obtained by normalizing the sum of the unit normal vectors of all triangles sharing cell i. A_m is the vector area of triangle m which has cell i as the vertex of the triangle.

$$E_Z = \sum_i \frac{1}{2} K_Z S_i d_{iz}^2 \qquad (9)$$

The constraint energy E_{Center} denotes the energy required by the model's assumptions on cell center and can be expressed with the constraint constant K_{Center} as follows:

$$E_{Center} = \frac{1}{2} K_{Center} \sum_i \| (x_i - x_i^{Center}) - [(x_i - x_i^{Center}) \cdot n_i] n_i \|^2 \qquad (10)$$

$$x_i^{Center} = \frac{1}{N_i} \sum_{j(i)} x_j \qquad (11)$$

Here, x_i^{Center} is the position vector of the center of mass of cell i where $j(i)$ below the summation symbol implies all the cells connected to cell i, and the number of these cells $N_i = \sum_{j(i)} 1$.

The model presented here includes dihedral energy (Eq. (6)) as a surrogate for the bending stiffness of the epithelial sheet. Variable θ_{eq} in Eq. (6) follows a normal distribution with a mean θ_{eq}^{ave} and standard deviation θ_{eq}^{SD}. This distribution reflects fluctuations in elastic energy in the cell height direction. Eq. (8) represents the repulsive interactions in effect only when the distance between two cells is smaller than r_c, reflecting the physical constraints due to the cell volume. Eq. (10) embodies the model's requirement that the position of a cell must coincide with the center of mass of its 2D shape on the normal surface plane (further details are provided in Appendix A).

To resolve Eq. (1), parameter values were normalized by unit length l, energy E_0, and time τ. Here l, E_0, and τ were set as $l = L_{eq}$, $E_0 = \frac{1}{2} K_L l^2$, and $\tau = 4\eta l^2 / E_0$, respectively.

2.3. Cell intercalation

During epithelial morphogenesis, cells can change their location either actively or passively. Cell rearrangements can be modeled as changes in the adhesion relationships between neighboring cells (Fig. 3(A)). In our model, cell rearrangements were simulated using flipping operations. The left panel of Fig. 3(B) shows a tetragon consisting of two triangles: one connecting cell 1, cell 2, and cell 3 and another connecting cell 1, cell 2, and cell 4. In this case, the term "flipping" refers to a procedure that erases the edge connecting cell 1 and cell 2, and draws a new one that connects cell 3 and cell 4 (Fig. 3(B), right). Flipping is performed only when the following conditions are met: (i) the distance between the center of mass of the two triangles before the operation (l_1) is smaller than the distance threshold l_{th} and (ii) l_1 is smaller than the new expected distance resulting from flipping (l_2). The position of the cell point remains unchanged with the flip. To avoid alternating between the same two diagonal lines continually, we introduced the concept of a "cooling time", in which a diagonal line drawn as a result of the flipping operation is fixed during the next τ_{ct} time.
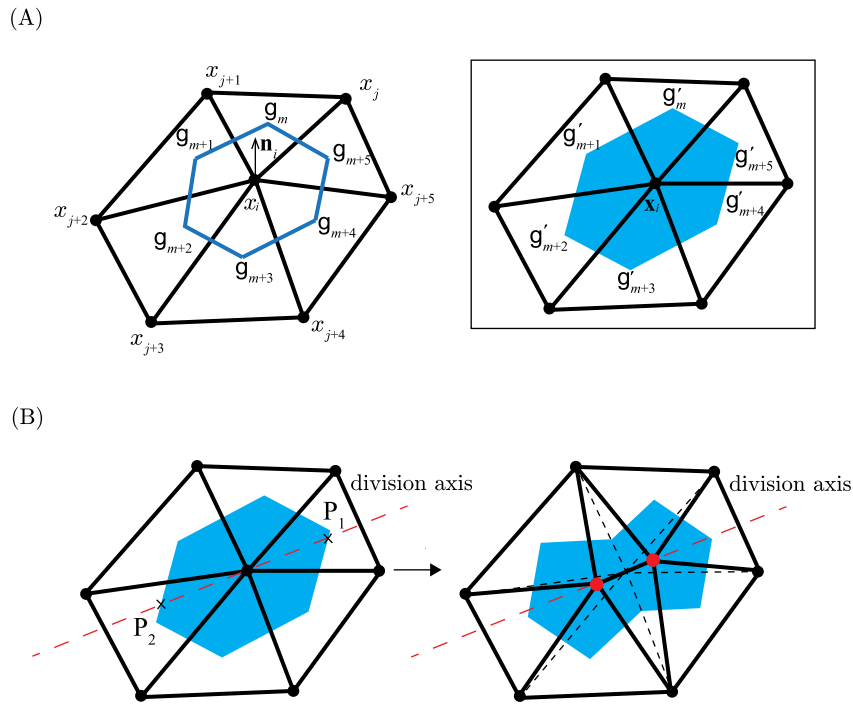
(A)

(B)

Fig. 4. Methods for the representation of cell division. (A) (left) The shape of cell i in 3D space is defined as a polygon consisting of the position vectors of the centers of mass of the triangles sharing cell i. Here, $\boldsymbol{g}_m$ represents the position vector of the center of mass of the triangle. (A)(right) Project $\boldsymbol{g}_m$ onto the plane normal to the normal vector of cell i, and let $\boldsymbol{g}'_m$ be the position vector after the projection. (B) (left) Finding the two intersection points, P_1 and P_2, between the projected polygon and the division axis that passes through $\boldsymbol{x}_i$. (B) (right) Setting the coordinates of the two cells after cell division so that the line segment $P_1 - P_2$ is internally divided in a 1:1:1 ratio. The dotted red line represents the axis of division. Cell i divides into two daughter cells. Red dots indicate newly formed cells.

2.4. Cell division modeling

The mathematical model for simulating cell division is based on Lomas model (Lomas, 2014); however, because Lomas model was developed for the bio-inspired artwork, we have improved it to take into account cell division orientation for use in biological studies as follows.

2.4.1. Geometry

The division of cell i was modeled geometrically. First, the cells directly linked to cell i are identified and projected onto a plane perpendicular to the surface-normal vector $\boldsymbol{n}_i$ at vertex i. Based on these projected points, a polygon is defined (Fig. 4(A)). The intersection points between the orientation axis of the division and polygon edges (which represent the cell shape) were then determined (Fig. 4(B), left). Finally, daughter cells were located at positions that divided the line segment internally in a 1:1:1 ratio (Fig. 4(B), right). Neighboring cells were re-linked to form a new network of triangles. Therefore, just after division, the two daughter cells are not necessarily the same size, nor are they necessarily half the size of the mother cell. However, the daughter cell is expected to be stable at the same size as the mother cell due to the triangular area elastic energy.

2.4.2. Interval

Based on previous studies (Okuda et al., 2013a; Inoue et al., 2017, 2020), we assumed that the timing of cell division fluctuates around the mean cell cycle time. More specifically, we hypothesized that cell i undergoes division when its post-division time τ_i reaches τ_i^{cycle}, where τ_i^{cycle} represents a random value with mean $\tau_{\text{ave}}^{\text{cycle}}$ and standard deviation $\tau_{\text{sd}}^{\text{cycle}}$ and satisfies the following:

$$\langle \tau_i^{\text{cycle}} \rangle = \tau_{\text{ave}}^{\text{cycle}} \tag{12}$$

$$\langle (\tau_i^{\text{cycle}} - \tau_{\text{ave}}^{\text{cycle}})(\tau_j^{\text{cycle}} - \tau_{\text{ave}}^{\text{cycle}}) \rangle = (\tau_{\text{sd}}^{\text{cycle}})^2 \delta_{ij} \tag{13}$$

where the symbol $\langle \cdots \rangle$ denotes the statistical mean and δ_{ij} is Kronecker's delta. In the default parameter settings, the post-division cell time randomly assumes a value ranging from zero to $\tau_{\text{ave}}^{\text{cycle}}$.

2.5. Apical constriction

The model described above does not include parameters that represent the 3D cell morphology. Hence, special modifications are needed to enable the model to describe apical constriction in a cell.

Apical constriction refers to the interactions between actin and myosin accumulated on the apical side of the cell (Martin and Goldstein, 2014), which causes the cell to become apically narrower by constriction (Fig. 5). Unlike 3D vertex models, our model does not allow intuitive expression of apical side cell contraction. In our model, the length of an edge projected onto the neutral surface of a cell represents the mean apical and basal lengths. Therefore, for an edge undergoing apical constriction, the energy of its projected edge between $\boldsymbol{g}_m$ and $\boldsymbol{g}_{m'}$ on the neutral surface can be described as Eq. (7) (see Fig. 5).

Additionally, apical constriction in one cell causes adjacent cells to change their orientation and lean towards it (Fig. 5(B)). These changes can be mathematically expressed using the dihedral angles. Specifically, the equilibrium dihedral angle θ_{eq} can be expressed as:

$$\theta_{\text{eq}} = \theta_{\text{eq0}} - \theta_{\text{apical}} \tag{14}$$

where θ_{eq0} and θ_{apical} represent the initial equilibrium angle and the changes resulting from apical constriction, respectively. In this study, we applied the addition of the energy (Eq. (7)) and the change in the equilibrium dihedral angle (Eq. (14)) to the edges to express that the entire apical surface shrinks.

3. Simulations

3.1. In-plane deformation

To confirm the effect of flipping, which represents cell rearrangement, we performed simulations under two conditions: (A) infrequent
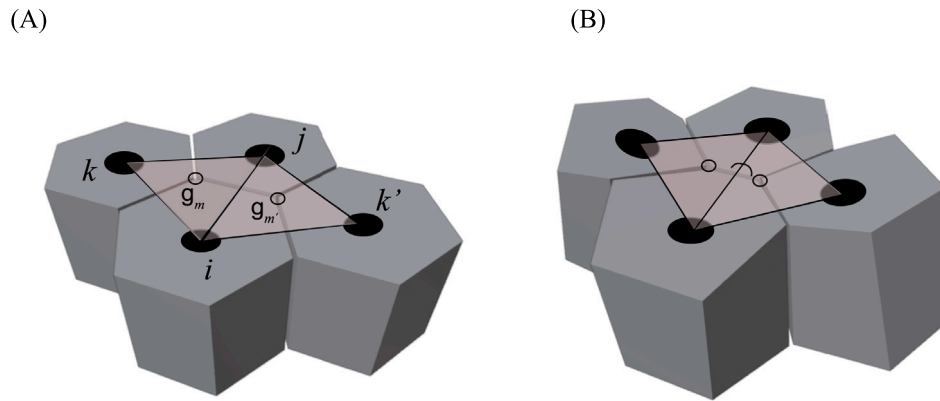
(A)   (B)

Fig. 5. Schematic of 3D cell shape shown in neutral cross-section. (A) Cells i, j, k, and k' are aligned in a plane before apical constriction. Cells i and j share the edge between g_m and $g_{m'}$. (B) The apical constriction of the edge between g_m and $g_{m'}$ decreases the length of this edge and also changes the dihedral angle between the two triangles by θ_{apical}.
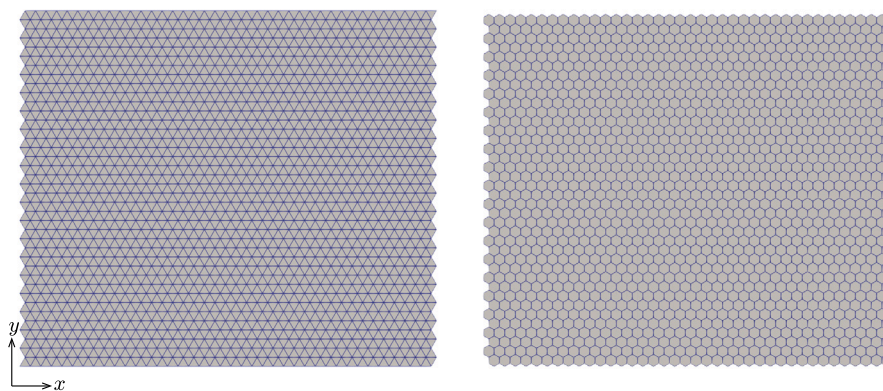

Fig. 6. Initial shape of the simulation. The calculation is based on a triangle mesh (left). Cell shape representation of left-hand figure (right).

flipping and (B) frequent flipping. First, simulations were conducted, in which the cell sheet was compressed forcefully in one direction and then relaxed. The differences in the time variation of the in-plane two-directional strain and final shape of the cell sheet were investigated. Further simulations were performed at multiple values of l_{th} to determine the relationship between l_{th}, the flip count, and the strain.

3.1.1. Computational conditions

We prepared a 40×40 cell sheet as shown in Fig. 6. The left panel of Fig. 6 shows the x–y plane projection of the initial state of the simulation model, which consisted of a layer of 1600 equilateral unit cells ($L_{\mathrm{eq}} = 1$) comprising 40 cells along both the x and y axes. The corresponding cell populations are shown in the right panel of Fig. 6 for the convenience of the reader. Computational simulations are performed on the points shown in the left panel of Fig. 6. Free boundary conditions were applied to all the boundary edges of the cell sheet.

Let $l_0 = L_{\mathrm{eq}}/\sqrt{3}$ be the length of the side of a regular hexagon, which is a 2D cell shape in its initial state (Fig. 6(right)). Two simulations were performed with different values of l_{th}/l_0: 0.606 and 0.745.

The y-coordinate of each cell point is forced to be displaced by a factor of α ($\alpha < 1$) at every step until $T_1 = 60$. In other words, y becomes αy at each computational step. Then, a relaxation simulation was performed until $T_2 = 160$ to calculate the strain in the x- and y-directions. The midpoint of the y-axis side of the cell sheet at the initial time was used as the y origin. To represent the cell sheet expanding in x direction caused by forced displacement in the y direction, for cells at the boundary of the cell sheet, the edge with the adjacent cell is

Table 1
Parameters for in-plane deformation simulations.

Symbol	Value	Description
α	0.99999	Forced-displacement magnification factor
η	0.25	Cell point friction coefficient
K_L	2	Edge length elasticity constant
K_S	10	Triangular area elastic constant
K_D	10	Dihedral angle elastic constant
K_Z	0	Out-of-plane deformation constraint constant
K_{Rep}	10	Cell repulsion constant
K_{Center}	10	Constraint constant
L_{eq}	1.0	Equilibrium edge length
L_{sep}	1.5	Separation length
A_{eq}	0.433	Equilibrium triangle area
$\theta_{\mathrm{eq}}^{\mathrm{ave}}$	3.14159	Statistical average of dihedral-angle equilibrium
$\theta_{\mathrm{eq}}^{\mathrm{SD}}$	0.02	Standard deviation of dihedral-angle equilibrium
r_c	0.9	Cut-off distance
l_{th}	0.25	Flip threshold length
Δt	0.0002	Integration time step
τ_{ct}	0.001	Flip cool time

removed when the distance to the adjacent cell exceeds a threshold L_{sep}. The other parameters are listed in Table 1. Euler's first-order method was used to integrate the equations of motion numerically. The computation time of some simulations is summarized in Supplementary S1.

3.1.2. Definition of strain

To calculate the strain, we obtained the length of the cell sheet by taking the cell average at each end of the cell sheet. During the initial placement, the cells at the edge of the sheet were marked and defined
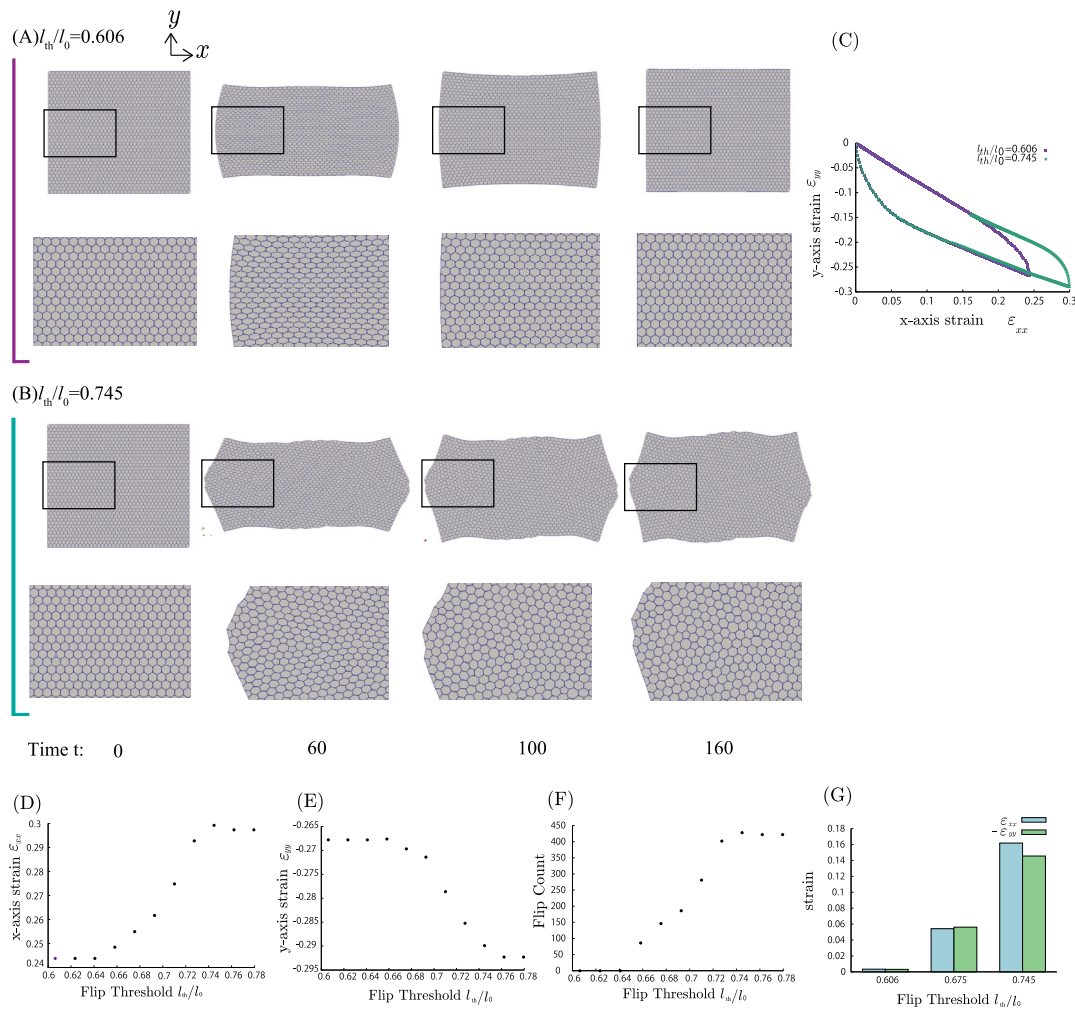
Fig. 7. Simulation results of out-of-plane deformation to confirm the effect of flips. (A) Simulation snapshot when no flips have occurred and (B) simulation snapshot after a sufficient number of flips have occurred. In both (A) and (B), the upper side is a snapshot of the entire image and the lower side is a magnified view of the rectangular area. (C) Evolution over time of the x- and y-directional strains. The purple dots indicate the values under condition (A) and the green dots indicate the values under condition (B). (D) and (E) The x- and y-directional strains at $t = 60$ and (F) the number of flips up to $t = 60$ for several values of l_{th}. (G) The x- and y-directional strains at $t = 160$.

as the set to be used in these calculations. These sets did not change over time. Let X_+ and X_- be the sets of cells initially at the right and left ends, respectively. Similarly, let Y_+ and Y_- be the sets of cells at the upper and lower ends, respectively.

The lengths in the x and y directions are calculated as follows:

$$L_x = \sum_{i \in X_+} x_i / N_{X_+} - \sum_{i \in X_-} x_i / N_{X_-} \tag{15}$$

$$L_y = \sum_{i \in Y_+} y_i / N_{Y_+} - \sum_{i \in Y_-} y_i / N_{Y_-} \tag{16}$$

Then, the strain in the x direction is $\epsilon_{xx} = (L_x - L_x^0)/L_x^0$, and strains in the y direction $\epsilon_{yy} = (L_y - L_y^0)/L_y^0$. L_x^0 and L_y^0 represent the initial sheet lengths in the x and y directions, respectively.

3.1.3. Results

To visualize the time evolution of the cell sheet shape under the two conditions ($l_{th}/l_0 = 0.606, 0.745$), the sheet shapes at the four time points are shown in Fig. 7(A) and (B). From left to right, $t = 0$, $t = 60$, $t = 100$, and $t = 160$. Moreover, $T_1 = 60$ is the state at the end of the forced displacement and $T_2 = 160$ is the state at the end of the relaxation. For those who are interested in detailed coordinate data, please refer to Supplementary data S2.

The cell sheet shape differed depending on the value of l_{th}. Under the condition $l_{th}/l_0 = 0.606$ (Fig. 7(A)), an elastic deformation that

returns the cell sheet to a shape close to the initial shape is dominant, whereas under condition $l_{th}/l_0 = 0.745$ (Fig. 7(B)), plastic deformation that does not return the cell sheet to the original shape after relaxation is dominant.

To visualize the difference in the quantitative sheet shape, the variation in the x- and y-directional strains over time is shown in Fig. 7(C). A difference in the ease of returning to the original shape was observed. The sheet shape is restored when l_{th}/l_0 is 0.606 but not when l_{th}/l_0 is 0.745.

Fig. 7(D)–(G) presents the results of similar simulations under more conditions. In Fig. 7(D) and (E), we demonstrate how the x and y directional strains at $t = T_1$ vary with respect to the value of flip threshold l_{th}. To confirm that the flip count varies with l_{th} up to $t = T_1$, the relationship between l_{th} and flip count is shown in Fig. 7(F). Flipping does not occur under condition (A) but occurs fully under condition (B). x-axis strain, y-axis strain, and flip count vary sigmoidally with respect to l_{th}. Fig. 7(G) shows the strain after mechanical relaxation($t = T_2$). The cell sheet clearly did not return to its original shape when l_{th} was large.

3.2. Out-of-plane deformation

The model developed in this study did not include a sheet thickness parameter. Instead, it employs a dihedral energy term to account for the
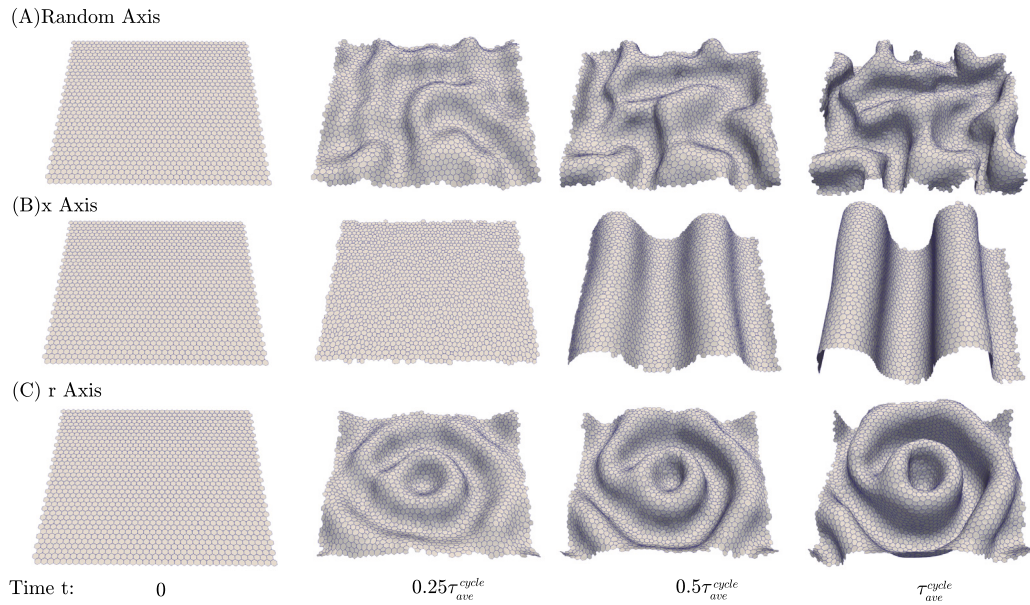
Fig. 8. Simulation snapshots when the axes of cell division are set to (A) random directions, (B) along the *x*-axis, and (C) in a radial direction from the center of the sheet.
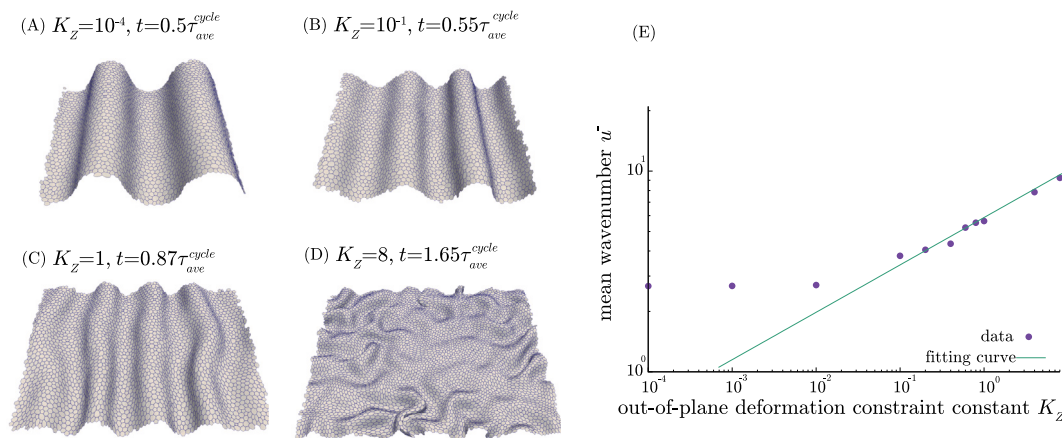

Fig. 9. Simulation snapshots of folding patterns at (A) $K_Z = 10^{-4}$, (B) $K_Z = 10^{-1}$, (C) $K_Z = 1$, and (D) $K_Z = 8$, respectively. (E) Wavenumber of wrinkles with respect to the strength of the out-of-plane deformation constraint.

effects of the sheet stiffness. Therefore, we evaluated the quantitative validity of the dihedral energy term. For this purpose, we present the results of simulations performed under the same conditions as those in the previous 3D vertex model (Inoue et al., 2020) and compared the results. First, we discuss whether the same folding patterns formed in the previous study were formed when the direction of the division axis was specified. Next, the effects of changes in the out-of-plane deformation constraint constant K_Z on the sheet-folding patterns are discussed.

3.2.1. Computational conditions

A cell sheet of 1600 cells was prepared as shown in Fig. 6. Periodic boundary conditions are used in this study.

To evaluate the folding structure quantitatively, we used $\bar{u}$ as in Inoue et al. (2020). $\bar{u}$ represents the mean wavenumber, which is determined using Fourier transform (See Supplementary materials S3 for details). In this study, we used the wavenumber observed when the difference between the point with the largest z coordinate and the point with the smallest z coordinate was larger than $\sqrt{2}L_{\text{eq}}$.

The other simulation parameters are listed in Table 2. Euler's first-order method was used to integrate the equations of motion numerically.

3.2.2. Results

We first examined the differences in the folding patterns in the direction of cell division. Fig. 8 shows the folding patterns when the axes of cell division are set to (A) a random direction, (B) the *x* direction, and (C) a radial direction from the center of the sheet. Different folding patterns were formed, depending on the axis of division. The wrinkles were formed perpendicular to the division direction.

Next, to investigate the relationship between the out-of-plane deformation constraint constant K_Z and wavenumber $\bar{u}$, simulations were performed for 12 different values of K_Z ($10^{-4}, 10^{-3}, 10^{-2}, 10^{-1}, 0.2, 0.4, 0.6, 0.8, 1, 2, 4, 8$) to obtain the wavenumbers. The results are presented in Fig. 9, where the cell division is allowed in the *x* direction. Fig. 9(A) to (D) show snapshots of folding patterns at $K_Z = 10^{-4}, 10^{-1}, 1$, and 8, respectively. As K_Z increased, the number of wrinkles increased. When K_Z is eight, wrinkles that are not orthogonal to the direction of division are also formed. Fig. 9(E) shows that the wavenumber representing wrinkles varies with the strength of the out-of-plane deformation constraint. This graph represents a double log plot. The plot points are the averages of the five simulations. In the figure, there are K_Z-dependent and K_Z-independent regions, and the power exponent in the K_Z-dependent region is 0.23, which is close to the theoretical value of 0.25 (Cerda and Mahadevan, 2003; Brau et al., 2013).

Table 2
Parameters for out-of-plane deformation simulations.

Symbol	Value	Description
η	0.25	Cell point friction coefficient
K_L	2	Edge length elasticity constant
K_S	10	Triangular area elastic constant
K_D	10	Dihedral angle elastic constant
K_Z	0–1	Out-of-plane deformation constraint constant
K_{Rep}	10	Cell repulsion constant
K_{Center}	10	Constraint constant
L_{eq}	1.0	Equilibrium edge length
A_{eq}	0.433	Equilibrium triangle area
θ_{eq}^{ave}	3.14159	Statistical average of dihedral-angle equilibrium
θ_{eq}^{SD}	0.02	Standard deviation of dihedral-angle equilibrium
r_c	0.9	Cut-off distance
l_{th}	0.25	Flip threshold length
Δt	0.0002	Integration time step
τ_{ave}^{cycle}	100	Statistical average of the cell cycle
τ_{sd}^{cycle}	1	Standard deviation of the cell cycle
τ_{ct}	0.001	Flip cool time

Table 3
Parameters for apical constriction simulations.

Symbol	Value	Description
η	0.25	Cell point friction coefficient
K_L	2	Edge length elasticity constant
K_S	10	Triangular area elastic constant
K_D	10	Dihedral angle elastic constant
K_Z	0	Out-of-plane deformation constraint constant
K_{Rep}	10	Cell repulsion constant
K_{Center}	10	Constraint constant
K_{apical}	10	Apical constriction constant
L_{eq}	1.0	Equilibrium edge length
A_{eq}	0.433	Equilibrium triangle area
θ_{eq0}^{ave}	3.14159	Statistical average of the dihedral-angle equilibrium
θ_{apical}	0.26	Variation of apical constriction
θ_{eq}^{SD}	0.02	Standard deviation of the dihedral-angle equilibrium
r_c	0.9	Cut-off distance
l_{th}	0.25	Flip threshold length
Δt	0.0002	Integration time step
τ_{ave}^{cycle}	20	Statistical average of the cell cycle
τ_{sd}^{cycle}	0.2	Standard deviation of the cell cycle
τ_{ct}	0.001	Flip cool time

3.3. Invagination caused by apical constriction

In this section, we perform simulations to examine the mathematical expressions of the apical constriction in our model.

3.3.1. Computational conditions

To evaluate the validity of Eqs. (7) and (14), we examined the following three mathematical expressions of apical constriction: (C1) Eq. (7) is used alone, (C2) Eq. (14) is used alone, and (C3) Eqs. (7) and (14) are employed.

Taking note of a previous study (Inoue et al., 2017), we employed the following spatial patterns of apical constriction: (A) Entire surface of the hexagon (Fig. 10(A)), and (B) Only the circumferential region of the same hexagon (Fig. 10(B)).

The initial state of the model was a square monolayer sheet of 400 cells, with 20 cells aligned along the x and y axes. The model used periodic boundary conditions and cell division occurred only within the outer hexagon of interest. Cell division was allowed in random directions. The simulation parameters are summarized in Table 3. The equations of motion were numerically integrated using Euler's first-order method.

3.3.2. Results

Fig. 11 presents snapshots taken at $t = \tau_{ave}^{cycle}$ for simulations under conditions (C1), (C2), and (C3). Cross-sectional views are obtained along the yellow line in Fig. 10. The results under condition (C1) show that the sheet remains flat at $t = \tau_{ave}^{cycle}$. Under condition (C2), both spatial patterns showed invagination in the same direction. Under condition (C3), invagination occurred in both spatial patterns, but in opposite directions.

4. Discussion

4.1. In-plane deformation

Elastic deformation occurs when the flip threshold is small and plastic deformation occurs when the flip threshold is large. This depends on the frequency of the cell rearrangement. We speculated that the reason for the results shown in Fig. 7(D), (E), and (F) are sigmoidal with respect to the flip threshold is that there is always mechanical relaxation, and the lengths of the edges are almost equal. Hence, the flips either do not occur at all, or they all occur under forced displacement. Additionally, the middle part tends to stretch because it cannot escape in the y-direction.

From Fig. 7(A), the cell sheet returned to a shape similar to the initial one in the time from $t = 60$ to $t = 160$ when no flip is occurring. The relaxation on the cellular scale may occur on a time scale of τ, while the relaxation on the tissue scale could be 100 times longer.

The phenomenon of forced displacement along the y-axis, which results in elongation along the x-axis, may be related to the mechanical essence of convergent extension. Convergent extension is a key process by which tissues narrow along one axis and extend along the other (Shindo et al., 2019; Tada and Heisenberg, 2012; Keller et al., 1992; Nishimura et al., 2012). Convergent extension involves two fundamentally different types of cell movement: collective cell migration, which typically represents the coordinated movement of highly aggregated cell sheets, and cell intercalation, which change the shape of the tissue through the directed exchange of neighboring cells (Tada and Heisenberg, 2012). Although our model considers the intercalation in contrast, collective cell migration was not included in the model. From a mechanical point of view, because collective cell migration provides the driving force for displacement of the cell sheet in the appropriate direction, the forced displacement condition in our simulation was thought to be similar to the displacement caused by collective cell migration. Because our model represents each cell as a particle, the self-propelled particle model proposed in previous studies (Akiyama et al., 2017; Vicsek et al., 1995) may be applied to the modeling of collective cell migration in future extensions of our model.

4.2. Out-of-plane deformation

The folding pattern according to the division axis orientation is consistent with previous studies using 3D vertex models. From mechanics and buckling theory, it is reasonable to expect that the wavenumber follows the power law. In the region where K_Z is large, the dependence of the wavenumber on K_Z follows a power law with a power exponent approaching to the theoretical value of 0.25 in the continuum. We speculate that the reason why some regions depend on K_Z and others do not is the magnitude of the relationship in the time scale between cell division and mechanical relaxation. At lower values of K_Z, the time scale of cell division is small compared with the time scale of mechanical relaxation, and wrinkles are formed only in the local mechanical field. This is confirmed by the fact that when the cell cycle is long, the region where the wavenumber is independent of K_Z shifts to the left (further details are provided in Appendix B).

Even in the K_Z-dependent region, the exponent was smaller than the theoretical value of 0.25. The size of the triangular element used in our model determines the minimum folding wavelength and causes the wavenumber to exhibit smaller increments at higher folding frequencies, folding is unlikely to occur at shorter wavelengths. Therefore, in the log–log plot, the slope is smaller at higher wavenumbers.
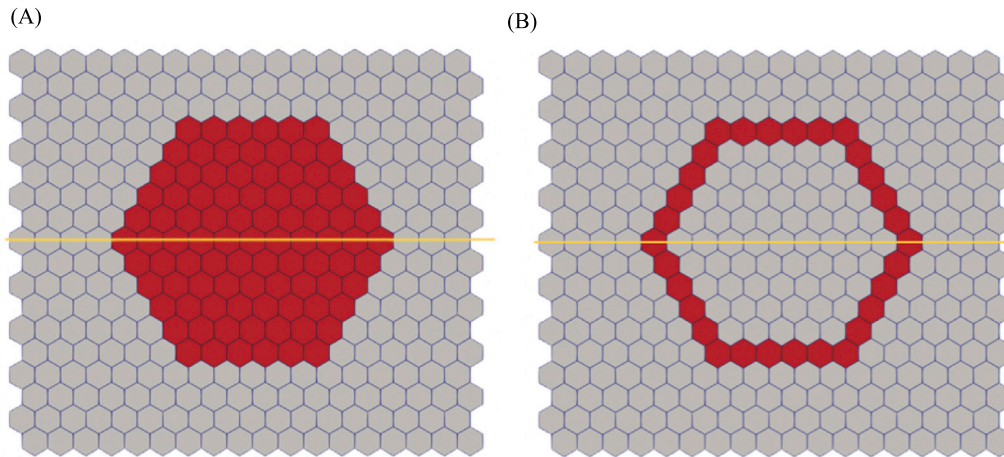
京都大学
KYOTO UNIVERSITY

T. Mimura and Y. Inoue

Journal of Theoretical Biology 571 (2023) 111560

京都大学学術情報リポジトリ
KURENAI 紅
Kyoto University Research Information Repository

Fig. 10. Two spatial patterns (A) the entire surface of a red colored hexagon, and (B) only the circumferential region of the same hexagon used in the simulations of apical constriction. The yellow line indicates the location of the cross section shown in Fig. 11. The red region indicates where apical constriction occurs.
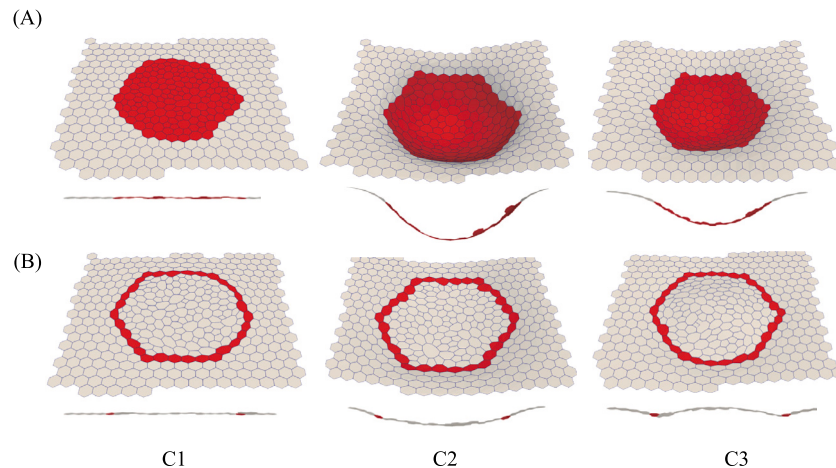

Fig. 11. Apical constriction occurred in (A) hexagonal region and (B) its circumference region. The cross section image below each figure is obtained along with the yellow line shown in Fig. 10. Snapshots taken at $t = \tau_{\text{ave}}^{\text{cycle}}$ under conditions of apical constriction expressed by (C1) Eq. (7) alone, (C2) Eq. (14) alone, and (C3) both Eqs. (7) and (14).

As shown in Fig. 9(A–D), the folding structures were strongly influenced by the cell division direction when the K_Z values were small ($K_Z < 1$); however, the effects gradually diminishes with an increase K_Z. Large K_Z values represent large forces restraining the out-of-plane deformation, which presumably caused the thin epithelial layer to fold into a complex and random manner that superseded the effects of the cell division direction.

4.3. Invagination caused by apical constriction

A major criterion used to evaluate the validity of apical constriction simulation is whether invagination is formed at the center of a hexagon. In a previous study using a 3D vertex model, the sectional view of the model was concave in the downward direction (basal side) for case (A) and concave in the upward direction (apical side) for case (B). This occurred only under condition (C3). The energy representing the apical constriction consists of two terms, and the results are consistent with the 3D vertex model (Inoue et al., 2017) only when these two terms are introduced.

No invagination occurred under condition (C1) because it only shortened the length of the sheet on the plane. By contrast, Eq. (14) bends the sheet, causing it to warp downward. In Fig. 11(B), the difference between the results for conditions (C2) and (C3) is due to the tension of the rings. Under condition (C2), the inner cell divides,

causing the ring to expand as it is pushed by the inner cell. Under condition (C3), the inner part of the ring exerts tension to keep the ring in place; hence, the inner part of the ring expands on the apical side.

As shown in Fig. 11(A), the amount of deformation was greater under condition (C2) than under condition (C3). Eq. (14) drives the bending of the sheet, whereas Eq. (7) flattens it. Interactions between these contradicting forces resulted in a smaller amount of deformation under condition (C3) than under condition (C2).

Although this model does not represent the 3D shape of the cell, it shows that the effect on tissue-scale deformation is equivalent to the change in the wedge shape of the cell owing to apical constriction.

4.4. The advantages and limitations of this model

In this model, the degrees of freedom in the cell height direction are eliminated, and each cell is represented by a cell center to reduce the degrees of freedom. In the case of Delaunay triangulation, a flip is necessary whenever it is required to guarantee the Delaunay property. However, using the center of mass of a triangle, the frequency of flips can be controlled by a threshold value, as shown in the in-plane deformation results. Addressing 3D deformations of monolayer epithelia, such as out-of-plane deformations, allows the model to be directly extended as a 2D curved surface embedded in 3D space. However, when

performing Delaunay triangulation on a curved surface, it is challenging to maintain the Delaunay–Voronoi duality while dealing with flips, as it is not possible to perform the process in the same way as on a flat plane.

However, using triangular centers of mass, the model cannot handle cell populations where individual cells are not uniform in size. It is not possible to represent conditions where the lengths of the sides of the polygons in the cell shape are too short. The approachable distance is limited as long as the triangle is not collapsed, as it is guaranteed to be inside a triangle. Regardless, the current model is limited to monolayer cell sheets and must be extended to handle multilayers and filled systems by adding a new energy function. Since cell height information is not included in the model, it cannot accommodate cell elongation. As shown in Fig. 1(B), the cell shape is determined only when the surrounding points are determined, and a scale smaller than Fig. 1(B) cannot represent the cell shape at all.

Because there is no reliable bottom-up or top-down method to determine cellular and tissue parameters in the model, the parameters used in this study were determined empirically. This is a common situation, as even the 3D vertex model, which discretely represents cells, faces similar challenges. To address this in the future, we will propose a new framework that uses data assimilation to determine biologically feasible parameter values in the model. By developing this framework, we can determine feasible parameter values, which would not be possible otherwise. Therefore, we have developed the proposed model that is computationally efficient.

Here, we compare our model with existing models. One such model is the Voronoi model (Saye et al., 2011). The 3D Voronoi model has been used to express multiphase of materials in computations, where the level set method is used to evolve the boundaries of each phase. Multiphase fluid flow simulations have been demonstrated using this model. Therefore, if the information on 3D cell shape is required in our model, the 3D Voronoi approach could be useful for recovering the 3D cell shape. However, extra effort is required to incorporate the 3D Voronoi model into our model. Because our model deals with monolayers, it is necessary to define a process such as placing cells virtually outside the plane when handling the 3D shape of cells as in the 3D Voronoi model. If the level set method were to be used in our model, the computation cost would become higher due to the computations of level set functions. Thus, if we were to use the 3D Voronoi model in conjunction with our model to express 3D cell shape, the 3D vertex model could be another candidate from the viewpoint of computational costs. The cell potts model (CPM) expresses multiple cell dynamics in the lattice site (Belmonte et al., 2016). Complicated interfaces among cells are spontaneously represented in terms of local minimization of energy; however, because CPM does not address the equation of cell center motion, it will be difficult to apply it directly to the purpose of data assimilation, as we intend to in the future. The 2D vertex model also expresses multiple cells dynamics (Farhadifar et al., 2007; Staple et al., 2010; Smith et al., 2012). In the vertex model, because the boundary edge between two adjacent cells is explicitly expressed, the computational costs of the vertex model is higher than that of our model. However, the model can be efficient to explain how the boundary edge play an important role in morphogenetic dynamics of tissue such as cell rearrangements by contractions (Shindo et al., 2019). Further, the 2D vertex model has been extended to recapitulate chemical signaling such as morphogen diffusions in terms of finite element method (FEM) on 2D mesh (Smith et al., 2012). Although our current model does not deal with chemical signals, we can use the FEM approach from the 2D vertex model as a starting point to introduce them into our model.

5. Conclusion

In our model, cells are represented as points, and interactions between adjacent cell points are considered. The cell shape was defined

as a polygon using the center of mass of adjacent triangles. Simulations using this model confirmed that our model can represent elastic to plastic deformation depending on the frequency of cell rearrangement and that cell proliferation causes sheet buckling, which is consistent with the power law derived based on continuum mechanics. However, because the present model cannot directly represent 3D cell shape changes such as the wedge-shaped 3D cell shape due to apical constriction, the relevant energy function was modeled to consider the effect of apical constriction in this study. The energy functions yielded results that were in qualitative agreement with the 3D vertex model results. This suggests that global tissue deformation can be handled by local cell force generation using the model. Because the model does not directly deal with the 3D shape of the cell, it succeeded in reducing the number of computational degrees of freedom and has the advantage of being computationally less expensive than the 3D vertex model when one is interested in the spill over of mechanical effects to the tissue scale rather than in the details of the 3D cell shape itself. This has the advantage that simulations using our model can be performed with less computational cost than those using a 3D vertex model. This is expected to open the way for hybridization using computationally expensive algorithms for sequential data processing, such as data assimilation.

CRediT authorship contribution statement

Tomohiro Mimura: Conceptualization, Methodology, Software, Investigation, Visualization, Writing – original draft. **Yasuhiro Inoue:** Conceptualization, Methodology, Supervision, Writing – review & editing, Funding acquisition.

Declaration of competing interest

None.

Acknowledgments

Appendix A. Constraint energy E_{Center}

Let the position vector x_i represent the coordinates of cell point i, which is surrounded by N cell points, whose coordinates are represented by vectors x_j, x_{j+1}, ..., and x_{j+N-1} in a counterclockwise manner. When we define g_m as the location of the center of mass of the triangle formed by vertices x_j, x_{j+1}, and x_i, it can be represented as follows: $g_m = \frac{x_j + x_{j+1} + x_i}{3}$. If we define g_{polygon} as the center of mass of the polygon whose vertices are the same as the triangle centers of mass g_m, g_{m+1}, ..., and g_{m+N-1}, then:

$$g_{\text{polygon}} = \frac{\sum_{m'=0}^{N-1} g_{m+m'}}{N}.$$

$$= \frac{x_i}{3} + \frac{2}{3} \frac{\sum_{j(i)} x_j}{N}$$

When $x_i = \sum_{j(i)} x_j / N$, the polygon center of mass coincides with the cell point i. Because our model is 3D, the above equation includes force-restraining out-of-plane deformation. To eliminate these effects, the components projected onto the plane perpendicular to the normal line n_i were used.

Appendix B. Cell cycle affects K_Z-dependence

To confirm that the cell division cycle affects K_Z dependence, we examined the K_Z dependence in five different cell cycles ($\tau_{\text{ave}}^{\text{cycle}} = 2, 10, 20, 100, 200, \tau_{\text{sd}}^{\text{cycle}} = \tau_{\text{ave}}^{\text{cycle}}/100$). The results are presented in Fig. B.1. A faster cell division cycle increases K_Z-independent regions. We believe that this is because the time constant of mechanical relaxation is long relative to the time scale of cell division, and hence, deformation occurs only according to the local field.
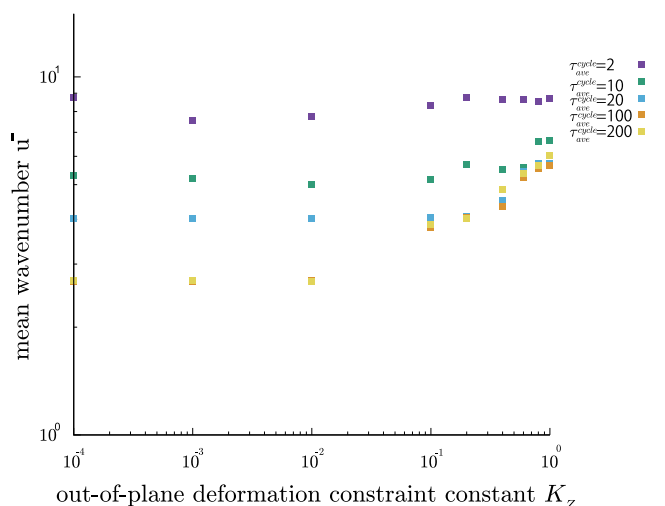
Fig. B.1. Relationship between out-of-plane deformation constraint constant K_Z and mean wavenumber in each cell cycle ($\tau_{\text{ave}}^{\text{cycle}} = 2, 10, 20, 100, 200, \tau_{\text{sd}}^{\text{cycle}} = \tau_{\text{ave}}^{\text{cycle}}/100$).

Appendix C. Supplementary data

Supplementary material related to this article can be found online at https://doi.org/10.1016/j.jtbi.2023.111560.

References

Adachi, H., Matsuda, K., Niimi, T., Inoue, Y., Kondo, S., Gotoh, H., 2018. Anisotropy of cell division and epithelial sheet bending via apical constriction shape the complex folding pattern of beetle horn primordia. Mech. Dev. 152 (June), 32–37. http://dx.doi.org/10.1016/j.mod.2018.06.003.

Akiyama, M., Sushida, T., Ishida, S., Haga, H., 2017. Mathematical model of collective cell migrations based on cell polarity. Dev. Growth Differ. 59 (5), 471–490. http://dx.doi.org/10.1111/dgd.12381, arXiv:https://onlinelibrary.wiley.com/doi/pdf/10.1111/dgd.12381.

Alt, S., Ganguly, P., Salbreux, G., 2017. Vertex models: from cell mechanics to tissue morphogenesis. Philos. Trans. Biol. Sci. 372 (1720), 20150520.

Antunes, M., Pereira, T., Cordeiro, J.V., Almeida, L., Jacinto, A., 2013. Coordinated waves of actomyosin flow and apical cell constriction immediately after wounding. J. Cell Biol. 202 (2), 365–379. http://dx.doi.org/10.1083/jcb.201211039.

Barton, D.L., Henkes, S., Weijer, C.J., Sknepnek, R., 2017. Active Vertex Model for cell-resolution description of epithelial tissue mechanics. PLoS Comput. Biol. 13 (6), 1–33. http://dx.doi.org/10.1371/journal.pcbi.1005569, arXiv:1612.05960.

Belmonte, J.M., Swat, M.H., Glazier, J.A., 2016. Filopodial-tension model of convergent-extension of tissues. PLoS Comput. Biol. 12 (6), e1004952.

Bi, D., Yang, X., Marchetti, M.C., Manning, M.L., 2016. Motility-driven glass and jamming transitions in biological tissues. Phys. Rev. X 6 (2), http://dx.doi.org/10.1103/PhysRevX.6.021011, arXiv:1509.06578.

Bonilla, L.L., Carpio, A., Trenado, C., 2020. Tracking Collective Cell Motion By Topological Data Analysis, Vol. 16, (12 December), arXiv:2009.14161, http://dx.doi.org/10.1371/journal.pcbi.1008407.

Brau, F., Damman, P., Diamant, H., Witten, T.A., 2013. Wrinkle to fold transition: influence of the substrate response. Soft Matter 9 (34), 8177–8186.

Brugués, A., Anon, E., Conte, V., Veldhuis, J.H., Gupta, M., Colombelli, J., Muñoz, J.J., Brodland, G.W., Ladoux, B., Trepat, X., 2014. Forces driving epithelial wound healing. Nat. Phys. 10 (9), 683–690. http://dx.doi.org/10.1038/NPHYS3040.

Cerda, E., Mahadevan, L., 2003. Geometry and physics of wrinkling. Phys. Rev. Lett. 90 (7), 074302.

Farhadifar, R., Röper, J.-C., Aigouy, B., Eaton, S., Jülicher, F., 2007. The influence of cell mechanics, cell-cell interactions, and proliferation on epithelial packing. Curr. Biol. 17 (24), 2095–2104. http://dx.doi.org/10.1016/j.cub.2007.11.049, URL: https://www.sciencedirect.com/science/article/pii/S0960982207023342.

Fletcher, A.G., Osterfield, M., Baker, R.E., Shvartsman, S.Y., 2014. Vertex models of epithelial morphogenesis. Biophys. J. 106 (11), 2291–2304. http://dx.doi.org/10.1016/j.bpj.2013.11.4498.

Honda, H., Tanemura, M., Nagai, T., 2004. A three-dimensional vertex dynamics cell model of space-filling polyhedra simulating cell behavior in a cell aggregate. J. Theoret. Biol. 226 (4), 439–453.

Inaki, M., Hatori, R., Nakazawa, N., Okumura, T., Ishibashi, T., Kikuta, J., Ishii, M., Matsuno, K., Honda, H., 2018. Chiral cell sliding drives left-right asymmetric organ twisting. ELife 7, e32506.

Inoue, Y., Suzuki, M., Watanabe, T., Yasue, N., Tateo, I., Adachi, T., Ueno, N., 2016. Mechanical roles of apical constriction, cell elongation, and cell migration during neural tube formation in xenopus. Biomech. Model. Mechanobiol. 15 (6), 1733–1746.

Inoue, Y., Tateo, I., Adachi, T., 2020. Epithelial tissue folding pattern in confined geometry. Biomech. Model. Mechanobiol. 19 (3), 815–822. http://dx.doi.org/10.1007/s10237-019-01249-8.

Inoue, Y., Watanabe, T., Okuda, S., Adachi, T., 2017. Mechanical role of the spatial patterns of contractile cells in invagination of growing epithelial tissue. Dev. Growth Differ. 59 (5), 444–454. http://dx.doi.org/10.1111/dgd.12374.

Keller, R., Shih, J., Sater, A., 1992. The cellular basis of the convergence and extension of the Xenopus neural plate. Dev. Dyn. 193 (3), 199–217. http://dx.doi.org/10.1002/aja.1001930302.

Lee, J.-Y., Harland, R.M., 2007. Actomyosin contractility and microtubules drive apical constriction in Xenopus bottle cells. Dev. Biol. 311 (1), 40–52.

Li, B., Sun, S.X., 2014. Coherent motions in confluent cell monolayer sheets. Biophys. J. 107 (7), 1532–1541. http://dx.doi.org/10.1016/j.bpj.2014.08.006.

Lomas, A., 2014. Cellular forms: An artistic exploration of morphogenesis. In: ACM SIGGRAPH 2014 Studio, SIGGRAPH 2014. http://dx.doi.org/10.1145/2619195.2656282.

Lowery, L.A., Sive, H., 2004. Strategies of vertebrate neurulation and a re-evaluation of teleost neural tube formation. Mech. Dev. 121 (10), 1189–1197.

Martin, A.C., Goldstein, B., 2014. Apical constriction: themes and variations on a cellular mechanism driving morphogenesis. Development (Cambridge) 141 (10), 1987–1998.

Meineke, F.A., Potten, C.S., Loeffler, M., 2001. Cell migration and organization in the intestinal crypt using a lattice-free model. Cell Prolif. 34 (4), 253–266.

Metzcar, J., Wang, Y., Heiland, R., Macklin, P., 2019. A review of cell-based computational modeling in cancer biology. JCO Clin. Cancer Inform. (3), 1–13. http://dx.doi.org/10.1200/cci.18.00069.

Murphy, S.V., Atala, A., 2014. 3D bioprinting of tissues and organs. Nature Biotechnol. 32 (8), 773–785. http://dx.doi.org/10.1038/nbt.2958.

Nishimura, T., Honda, H., Takeichi, M., 2012. Planar cell polarity links axes of spatial dynamics in neural-tube closure. Cell 149 (5), 1084–1097. http://dx.doi.org/10.1016/j.cell.2012.04.021.

Okuda, S., Inoue, Y., Eiraku, M., Sasai, Y., Adachi, T., 2013a. Modeling cell proliferation for simulating three-dimensional tissue morphogenesis based on a reversible network reconnection framework. Biomech. Model. Mechanobiol. 12 (5), 987–996.

Okuda, S., Inoue, Y., Eiraku, M., Sasai, Y., Adachi, T., 2013b. Reversible network reconnection model for simulating large deformation in dynamic tissue morphogenesis. Biomech. Model. Mechanobiol. 12 (4), 627–644.

Osborne, J.M., Walter, A., Kershaw, S.K., Mirams, G.R., Fletcher, A.G., Pathmanathan, P., Gavaghan, D., Jensen, O.E., Maini, P.K., Byrne, H.M., 2010. A hybrid approach to multi-scale modelling of cancer. Phil. Trans. R. Soc. A 368 (1930), 5013–5028. http://dx.doi.org/10.1098/rsta.2010.0173.

Pathmanathan, P., Cooper, J., Fletcher, A., Mirams, G., Murray, P., Osborne, J., Pitt-Francis, J., Walter, A., Chapman, S.J., 2009. A computational study of discrete mechanical tissue models. Phys. Biol. 6 (3), http://dx.doi.org/10.1088/1478-3975/6/3/036001.

Romanazzo, S., Nemec, S., Roohani, I., 2019. iPSC bioprinting: Where are we at? Materials 12 (15), 2453.

Saye, R.I., Sethian, J.A., Lawrence Berkeley National Lab. (LBNL), C.U.S., 2011. Voronoi Implicit Interface Method for computing multiphase physics. Proc. Natl. Acad. Sci. - PNAS 108 (49), 19498–19503.

Shindo, A., Inoue, Y., Kinoshita, M., Wallingford, J.B., 2019. PCP-dependent tran-scellular regulation of actomyosin oscillation facilitates convergent extension of vertebrate tissue. Dev. Biol. 446 (2), 159–167. http://dx.doi.org/10.1016/j.ydbio.2018.12.017.

Smith, A.M., Baker, R.E., Kay, D., Maini, P.K., 2012. Incorporating chemical signalling factors into cell-based models of growing epithelial tissues. J. Math. Biol. 65 (3), 441–463.

Soumya, S.S., Gupta, A., Cugno, A., Deseri, L., Dayal, K., Das, D., Sen, S., Inamdar, M.M., 2015. Coherent motion of monolayer sheets under confinement and its pathological implications. PLoS Comput. Biol. 11 (12), http://dx.doi.org/10.1371/journal.pcbi.1004670, arXiv:1507.06481.

Staple, D.B., Farhadifar, R., Röper, J.., Aigouy, B., Eaton, S., Jülicher, F., 2010. Mechanics and remodelling of cell packings in epithelia. Eur. Phys. J. E Soft Matter Biol. Phys. 33 (2), 117–127.

Szabó, B., Szöllösi, G.J., Gönci, B., Jurányi, Z., Selmeczi, D., Vicsek, T., 2006. Phase transition in the collective migration of tissue cells: Experiment and model. Phys. Rev. E 74 (6), 061908.

Tada, M., Heisenberg, C.P., 2012. Convergent extension: Using collective cell migration and cell intercalation to shape embryos. Development (Cambridge) 139 (21), 3897–3904. http://dx.doi.org/10.1242/dev.073007.

Vicsek, T., Czirók, A., Ben-Jacob, E., Cohen, I., Shochet, O., 1995. Novel type of phase transition in a system of self-driven particles. Phys. Rev. Lett. 75, 1226–1229. http://dx.doi.org/10.1103/PhysRevLett.75.1226, URL: https://link.aps.org/doi/10.1103/PhysRevLett.75.1226.